Long-term assessment of cutaneous inflammation and treatment using optical resolution photoacoustic microscopy

YUANLONG ZHAO,[1] TINGTING LI,[1,4,†] HENG GUO,[1] RUI HU,[2] AND LEI XI[1,3,5,†]

[1]*Department of Biomedical Engineering, Southern University of Science and Technology, Shenzhen, Guangdong, 518055, China*
[2]*State Key Laboratory of Radio Frequency Heterogeneous Integration (Shenzhen University), College of Physics and Optoelectronic Engineering, Key Laboratory of Optoelectronic Devices and Systems of Ministry of Education and Guangdong Province, Shenzhen University, Shenzhen 518060, China*
[3]*Guangdong Provincial Key Laboratory of Advanced Biomaterials, Southern University of Science and Technology, Shenzhen, Guangdong 518055, China*
[4]*11930694@mail.sustech.edu.cn*
[5]*xilei@sustech.edu.cn*
[†]Co-corresponding authors

Abstract: Cutaneous inflammation is an acute skin disease characterized by edema and vascular hyperplasia. Longitudinal monitoring of vasculature is crucial for studying the development of inflammation and evaluating the therapeutic efficacy of drugs. Optical-resolution photoacoustic microscopy (OR-PAM) is a hybrid imaging tool for non-invasive and label-free visualization of microcirculations with a capillary-scale spatial resolution. In this study, we assess the feasibility of OR-PAM for long-term monitoring of vascular changes in 12-O-Tetradecanoylphorbol-13-Acetate (TPA)-induced mouse models, as well as the corresponding treatment process. Quantitative vascular evaluation is conducted based on derived key parameters, including vessel length, branchpoint number, vessel area fraction, vessel diameter, fractal dimension, vessel tortuosity and ear thickness, which reveal that vascular morphological changes are highly dependent on the concentration of TPA and existence of therapeutic drugs. Furthermore, the results show the potential of OR-PAM in the clinical management of inflammation and as an effective tool to evaluate vascular responses to pharmacological interventions *in vivo*.

1. Introduction

The skin forms an active barrier that provides the first line of immunological defense against exogenous irritants and infectious agents. The skin response to external infection is mediated by a highly sensitive and well-coordinated system, predominantly composed of blood vascular networks [1,2]. Since the microvasculature inside the skin facilitates the delivery of nutrients and transportation of oxygen to meet the metabolic demands of surrounding cells, it plays a pivotal role in both healthy and pathological states [3]. However, once the skin barrier is damaged, inflammation, which is dominated by the response of the vascular system, will form. Hence, the investigation of cutaneous inflammation holds paramount significance, due to the clinical relevance of inflammatory responses to various dermatological diseases including psoriasis, atopic dermatitis, and contact dermatitis. Understanding the role of blood vessels during the occurrence and progression of skin inflammation can guide the implementation and evaluate the effect of therapeutic strategies, so as to alleviate symptoms and prevent exacerbations of patients [4]. In this study, we focus on chemicals-induced cutaneous inflammation manifested by vascular leakage, regression, proliferation, and remodeling, as well as skin edema. Since the vascular structure is intimately linked to biological functions, long-term monitoring of vascular

morphological changes, including degeneration and angiogenesis, through non-invasive imaging methods can provide evidence of altered physiological states. Especially, the quantitative analysis of vascular changes has the potential to assist clinical diagnosis of inflammation progression, and provide an evaluation tool for anti-inflammatory therapy. Additionally, studies have shown that there is a connection between inflammation and tumor [5]. Hence, quantifying vascular changes in inflammation through imaging might help to analyze the complex relationship between inflammation and tumor, and further guide the cancer therapy.

Enzyme-linked immunosorbent assay (ELISA), with high sensitivity and accuracy, is a widely recognized method for assessing inflammation development [6]. However, this method requires complex tissue handling, fixation and staining procedures, and is prone to diagnostic errors due to non-standard operations [7]. Most importantly, these time-consuming procedures can only be conducted invasively, thus precluding observations of longitudinal dynamics for the same animal. In recent years, numerous *in vivo* imaging methods have been developed to monitor the changes in vascular parameters for diagnosing and assessing cutaneous inflammation. Intravital microscopy techniques, such as confocal laser scanning microscopy (CLSM), multiphoton microscopy (MPM), and optical coherence tomography (OCT), can visualize inflammation progression and treatment outcomes with a high resolution [8,9]. However, these methods are restricted by one or more limitations including the requirements of exogenous contrast agents, small field of views (FOVs), slow imaging speed and time-consuming data acquisition and computation. Longitudinal label-free visualization of vasculature changes in inflammatory skin can be realized by laser speckle contrast imaging (LSCI) and sidestream dark field (SDF) imaging [10,11]. Nevertheless, the angiogenesis process of reconstructed capillaries could not be detected by these two methods due to the limited spatial resolution and specificity. Consequently, there is an urgent demand for a large FOV, high resolution and high-speed imaging method to facilitate the long-term non-invasive quantitative evaluation of skin inflammation. Optical-resolution photoacoustic microscopy (OR-PAM) is a hybrid imaging modality that integrates the merits of optical and ultrasound imaging [12]. Owing to the capillary-scale spatial resolution, centimeter-scale FOV and real-time imaging capability, OR-PAM meets the aforesaid demands. In addition, OR-PAM can enable label-free, high signal-to-noise ratio and high sensitivity imaging of vascular networks using intrinsic optical absorption of endogenous hemoglobin and 100% relative sensitivity to small optical absorption changes [13,14,15]. Thus, the changes in vascular networks caused by chemicals-induced inflammation can be investigated under unperturbed physiological conditions.

Previous studies have reported variations in vascular parameters during lipopolysaccharide-induced vascular leakage and wound healing processes using OR-PAM [7,16,17]. In this work, we extended the study to the long-term (14 days) continuous monitoring of a newly constructed 12-O-Tetradecanoylphorbol-13-Acetate (TPA)-induced mouse ear inflammation model, as well as the anti-inflammatory treatment based on geraniol and indomethacin. TPA is a distinguished promoting agent for understanding vascular changes associated with skin inflammation [18]. A new TPA-induced skin inflammation mouse model has been established. Geraniol and indomethacin have been investigated to significantly inhibit TPA-induced inflammatory responses by promoting the release of proinflammatory cytokine [6,19]. To ensure the scientific rigor and validity of the experimental results, two well-designed modules were employed to assist imaging and drug administration. In order to intuitively track the dynamic changes in ear inflammation with different concentrations of TPA and the anti-inflammatory effects of different drugs (geraniol and indomethacin), seven vascular structure parameters, including mean and maximum vessel diameter (VD1 and VD2), vessel tortuosity (VT), vessel area fraction (VAF), vessel length (VL), branchpoint number (BN), and fractal dimension (FD), were extracted and quantitatively analyzed for OR-PAM images [20,21]. Notably, we have expanded the quantification to encompass a broader range of vessel parameters compared to the previous study [17]. Multiple training sets were established based on manually labeled images and the data augmentation method to train

the U-Net, thereby achieving enhanced accuracy in the segmentation of vascular systems across different groups and stages. Continuous monitoring of the mentioned vascular parameters can also offer a more comprehensive understanding of the inflammation process, in contrast to relying solely on selected observing time points. In summary, this study verifies the feasibility and accuracy of OR-PAM in long-term observation of inflammation and the anti-inflammatory effects of therapeutic drugs. Our results suggest that OR-PAM can be a promising tool for non-invasive and quantitative evaluation for inflammation responses, and also has prospective application in improving clinical diagnosis and treatment.

2. Materials

2.1. Photoacoustic imaging system and customized modules

The long-term monitoring of inflammatory skin regions was performed using an established OR-PAM system (VIS-50, PAOMTek Shenzhen, China). The imaging system has a lateral resolution of 10 μm and a FOV of 10 mm [22]. A 532 nm laser with a pulse repetition frequency of 50 kHz was employed to generate photoacoustic signals, which resulted in a single experimental time of 20 seconds. Prior to each experiment, the pulse energy at the imaging end was measured as 700 nJ.

To ensure uniform inflammation induction in the mouse ear, we devised and fabricated a customized resin module (Fig. 1(A)). Screws A and B within the mouse mount enabled fine-tuning of adjustable modules for vertical alignment, which guaranteed the mouse ear maintaining level while allowing unobstructed breathing during the drug administration. Medical gauze served as a medium between the ear-fixing module and mouse mount to distribute the drug consistently on the mouse ear. The underside of the ear fixing module (Fig. 1(B)) slightly compressed the medical gauze, facilitating uniform drug distribution. Twenty-four pinholes, each with a diameter of 0.05 mm, were symmetrically distributed on each side of the module, enabling drug delivery to the medical gauze and mouse ear skin. The number of holes was minimized to reduce the volatilization and photodecomposition of drugs. We conducted tests to verify that the drug dropping module applied minimal pressure to flatten mouse ears without distorting blood vasculature.

Furthermore, to enhance comprehensive imaging and reduce external interference with vascular parameters, an additional custom-designed 3D-printed module was engineered (Fig. 1(C)). Due to the structural properties of the mouse ear, flattening the auricle on the imaging plane using swabs is essential but can inevitably lead to vasculature damage and healing process disruption. To mitigate such effect, the ear-fixing rod applied gentle pressure to opposing sides of the auricle, leveling the curved end and ensuring a better fit to the imaging plane.

2.2. Chemicals and reagents

TPA (RHAWN, Shanghai, China), geraniol (GLPBIO, Montclair, USA), indomethacin (GLPBIO, Montclair, USA), and Dimethylsulfoxide (DMSO, PYTHONBIO, Guangzhou, China) were properly stored before the experiments. TPA was dissolved in DMSO immediately and divided into the concentration of 0.15, 0.3, and 0.45 g/L, designated as TPA I, II, and III. Geraniol and indomethacin were dissolved in DMSO at concentrations of 25 g/L and 3.6 g/L.

2.3. Experimental protocols

Female BALB/c mice (GemPharmatech, Nanjing, China), aged 8-10 weeks (~20 g), were utilized in this study. Mice were housed at a consistent and appropriate temperature ($24°C \pm 2°C$) under a 12-hour light-dark cycle with free access to standard food and water. Mouse ear hair was gently removed in advance to ensure clear visualization. After 24 hours, the mouse was maintained under gaseous anesthesia using 1.5% inhaled isoflurane and properly positioned in the adjuvant
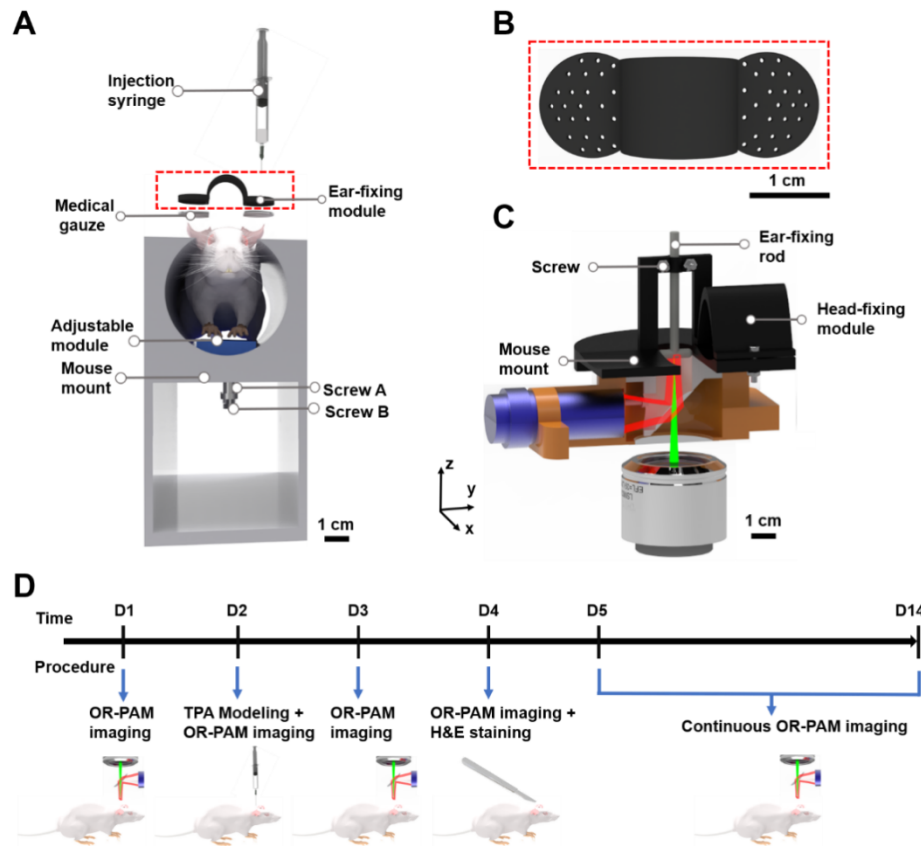
Fig. 1. Experimental materials and methods for OR-PAM-monitored ear inflammation. (A) Schematic of the adjuvant inflammation module. (B) Magnified picture of the adjuvant drug dropping module indicated by the dashed box in (A). (C) Schematic of auxiliary imaging module used in conjunction with the imaging interface of OR-PAM. (D) The protocol of TPA inflammation experiment.

imaging module, where a thin layer of ultrasonic coupling agent was applied to the imaging interface, as depicted in Fig. 1(C). Cranial positioning was secured by adjusting screws along the z-axis around the head-fixing module. Fine-tuning screws around the ear-fixing rod allowed manual adjustment of the y-position of the rod to accommodate different ear sizes and prevent auricles bending. Additionally, rotating the rod along the z-axis enabled the 1 cm-long cylindrical end to cover the entire ear area, effectively eliminating wrinkles and bubbles beneath the skin. Following the baseline (i.e., pre-inflammation) images acquisition, mice were transferred to an adjuvant inflammation module. Throughout the imaging and inflammation period, the body temperature was maintained at 37°C with a heating pad on the mouse mount.

TPA-induced inflammation experiment and the anti-inflammatory treatment experiment were conducted with the experimental process illustrated in Fig. 1(D). On day 2, in the TPA-induced inflammation experiment (n = 24), mice were randomly and equally divided into four groups: control, group I, group II, and group III. The control group was administered with 20 μL normal saline, while group I to III were treated with 20 μL TPA I, II and III on the right ear, respectively. In the anti-inflammatory treatment experiment (n = 24), four randomly and equally divided groups were designated as Control, Model, GOH (the group treated with geraniol), and Indo (the group treated with indomethacin). Control group: the surface of mouse ear was given 20 μL normal

saline; Model group: the surface of mouse ear was given 20 μL TPA III; GOH group: 25 μL geraniol was applied to the ear of mouse 30 minutes before applying 20 μL TPA III; Indo group: 40 μL indomethacin was administered to the ear of mouse one hour after applying 20 μL TPA III.

On day 4, one mouse from each group in both experiments was sacrificed, and the right ear was harvested and fixed in 4% paraformaldehyde at 4°C for histological study. Cross-section hematoxylin and eosin (H&E) staining was applied to the histology sections. During the 14-day experiment, the ear thickness was measured daily using a vernier caliper to quantify the extent of ear edema. The mean value was calculated to quantify the inflammation degree.

All the mice were sacrificed after experiments. All the experimental protocols were approved and supervised by the Animal Ethics Committee at the Southern University of Science and Technology.

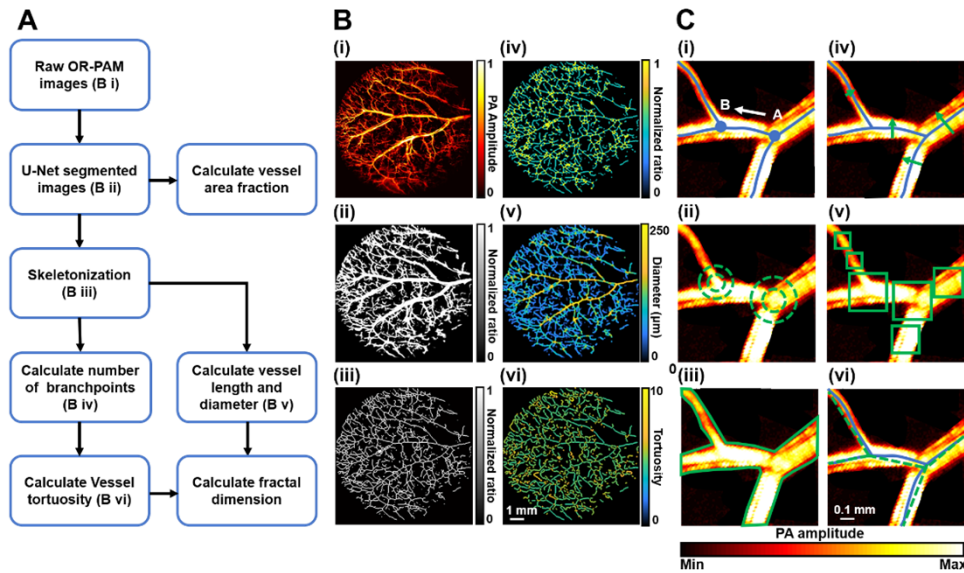### 2.4. Image processing and quantitative analysis of vascular parameters

The overall flowchart detailing the quantitative evaluation of vessel parameters was presented in Fig. 2(A), encompassing both morphological evaluation and blood vessel parameters assessment. It was noteworthy that the maximum amplitude projection (MAP) images were utilized as the primary image source (Fig. 2(B) (i)). Initially, training sets were established *via* manual segmentation of MAP images obtained from different experimental groups. During the process, image cropping was carried out to do data augmentation. After dividing the manually segmented images into 9, 16, or 25 equal parts, augmentation of the training sets was achieved by randomly shuffling and reassembling the segments. Then the raw MAP images were subjected to blood vessel area segmentation using a U-Net model trained on the aforementioned sets, as illustrated in Fig. 2(B) (ii) [23]. Specifically, the U-Net was featured by the cross-entropy loss function and the Adam optimizer [24]. The accuracy of the U-Net in blood vessel segmentation was defined as (*true positive + ture negative*)/ *N* , where *N* was the total number of the labels and the accuracy was calculated as 0.9516 [25]. The probability of a given region being identified as a vessel increases as the corresponding value approaches one. Subsequently, the skeleton of vasculature was extracted (Fig. 2(B) (iii)), documenting the path of blood vessels. Utilizing the skeletonized images, the branchpoints between two vascular branches were labeled with a brighter color to differentiate from vascular skeletons, as shown in Fig. 2(B) (iv). The skeletonized vascular image was then employed to establish the distributions of vascular diameter and tortuosity throughout the vascular framework, presenting a visual overview. The gradient hues within the color bar serve as a visual aid to depict dynamic fluctuations of the parameter.

2.5. Vessel parameters

The intricate and interconnected architecture of the vasculature inside the mouse ear poses a formidable obstacle for comprehending and delineating alterations in vessel morphology *via* a singular metric. To address this challenge, an array of parameters has been utilized to capture the unique characteristics of the vasculature. These parameters can be associated with a wide range of biological behaviors, including blood vessel growth, dilation, and permeability, therefore providing elucidation into the physiologic and pathological functions of the vascular system [26]. In this study, we derived six key vessel parameters including VL, BN, VAF, VD, FD, and VT.

VL is defined as the longitudinal dimension of vessel centerlines or vessel skeletons, and serves as a crucial parameter in evaluating spatial vessel density and potential anomalies in nutrient delivery mechanisms. During the quantification of VL, as depicted in Fig. 2, the cumulative summation of lengths between the starting and ending points in each vessel segment contributes to the total VL. Branchpoint signifies the termination of a vessel segment, where it bifurcates into two or more branches. BN serves as an index of the vascular network's interconnectivity and the quantity of arborizations. This metric can supply information regarding the network's resilience to occlusion or obstruction. VAF corresponds to the proportion of blood vessel area

Fig. 2. Quantitative analysis of OR-PAM images. (A) Overall flow chart of the algorithm for quantification of inflammation. (B) Representative images of each step in the images processing procedure: (i) MAP image; (ii) U-Net segmented image; (iii) skeletonization; (iv) branchpoint image; (v) vessel diameter map; (vi) vessel tortuosity map. (C) Visualization of basic parameters quantifying the morphological information of vasculature: (i) vessel length (A: starting points; B: ending points); (ii) number of branchpoints; (iii) vessel area fraction; (iv) vessel diameter; (v) fractal dimension; (vi) vessel tortuosity.

over the imaging area. The computation was executed on the binarized images. It ascertains the spatial vessel density that incorporates vessel thickness. For the points on the vasculature skeleton, the Euclidean distance between edge lines orthogonal to the centerline is defined as the vessel diameter. VD1 is calculated as the numerical average length of the normal line, while VD2 represents the distance for the widest point of the vessel lumen. VD1 reflects the characteristics of thin veins, arteries, and capillaries, while VD2 reveals the characteristic of the central artery due to its highest caliber. The combination of both parameters reflects the radial thickness of vessels, revealing the tendency and condition of vascular dilation, constriction, and remodeling. The box-counting method is employed to approximate the fractal dimension by overlaying the binarized images with a grid of boxes with side lengths of r and denoting the number of nonempty boxes as $N(r)$. Starting with a single pixel box encompassing the entire image, r was gradually decreased by a factor of two at each iteration, and the corresponding counts of non-empty boxes were tailed. Linear regression was performed to obtain the slope of the double logarithmic plot $\log N(r)$ versus $\log(1/r)$. FD is determined by $FD = \log N(r)/\log(1/r)$ [27]. This method identifies repeating structures of blood vessels across the range of scales and infers the vascular complexity. A measure of tortuosity provides the ratio of the actual vascular path length (arc length) to the linear distance (chord length) between two branchpoints [28]. The definition expression is formulated as $VT =$ Arc length/Chord length. The result is a dimensionless number reflecting the bending of the vessel segment. This metric indicates different process of vessel regression and remodeling.

2.6. Statistical analysis

The statistical analysis was performed by GraphPad Prism (9.5.1, GraphPad Software, Boston, USA), MATLAB (R2022a, The MathWorks, Natick, USA), and OriginPro (OriginLab, Northampton, USA). Every parameter was calculated based on five full-sized images and the numerical results were represented as mean value ± standard deviations. The normality of the data was assessed based on the Kolmogorov-Smirnov test. To determine statistical significance between two experimental groups, an unpaired t-test or one-way analysis of variance (ANOVA) was performed with a significance level set at $p < 0.05$.

3. Results

3.1. TPA-induced cutaneous inflammation experiment

In accordance with the inflammation experiment protocols outlined in section 2.3, we conducted *in vivo* imaging and verification with color photographs and H&E staining. As demonstrated in Fig. 3(A), representative OR-PAM images captured on days 1, 4, 9, and 14 clearly delineate differences in vascular morphology between different groups. These timepoints delineate distinct stages of the inflammatory process. Specifically, day 1 signifies the initial pre-inflammatory stage, day 4 corresponds to the inflammation summit, day 9 indicates the anti-inflammatory and healing process, and day 14 marks the culmination of the inflammatory response. We observed increased vessel dilation and capillary angiogenesis in correlation with higher concentrations of TPA. Notably, on day 4, subcutaneous hemorrhage (the hot spots and red shading in OR-PAM images) and vascular injury (the signal loss along the vasculature in OR-PAM images) were particularly pronounced, especially in group III. This phenomenon is attributed to the formation of blood clots at the inflammatory site and debris clearance from the damaged tissue, which in turn triggers the generation of mediators by cells in the vicinity of the inflammation. These mediators orchestrate a complex set of processes against inflammation, corresponding to the increased fill fraction of vessels that function to promote blood oxygen levels on day 9. The progress of angiogenesis was found to increase from Group I to III in proportion to the inflammation degree, as well as the strength of the immune response. On day 14, the overview and zoom-in images of the same vascular site were presented to facilitate overall and local comparisons between different groups. Our results confirm that different concentrations of TPA generate variations in vessel structures and functions.

Representative *ex vivo* color photographs (Fig. 3(B)) and H&E staining (Fig. 3(C)), as mentioned in section 2.3, were collected on day 4 for auxiliary validation. Figures 3(B) (ii-iv) reveals progressively severe redness, psoriasis, and hemorrhage of ears with the increasing concentration of TPA. Conversely, Fig. 3(B) (i) shows the morphology of normal ear, serving as the image of the control group. Subsequently, cross-section H&E staining of ear sections reveals histological differentiation caused by TPA. Epidermal hyperplasia (indicated by the orange arrow), neutrophil infiltration (indicated by the blue arrow), and tissue edema (indicated by the black arrow) are labeled as hallmarks for evaluation. Our analysis reveals considerable increases in tissue swelling, dense inflammatory cell infiltration, and epidermal hyperplasia in the TPA-induced ear inflammation groups. By contrast, no conspicuous mutations are observed in the control group (Fig. 3(C) (i)), which is consistent with the *in vivo* monitoring results in Fig. 3(A).

Subsequently, we performed statistical analyses of OR-PAM images to make quantitative comparisons between different experimental groups (Fig. 4). The variation curves in Fig. 4(A) record the progression of vessel parameters throughout the 14-day experimental cycle. Mean and maximum vessel diameter (Figs. 4(A) (i-ii)) exhibit a marked increase in the initial three days, and reach their peak on day 2 and 3, respectively, indicating the disappearance of capillaries and vascular dilation of ears. Of note, group III displays the most substantial expansion ratio (41.8%,
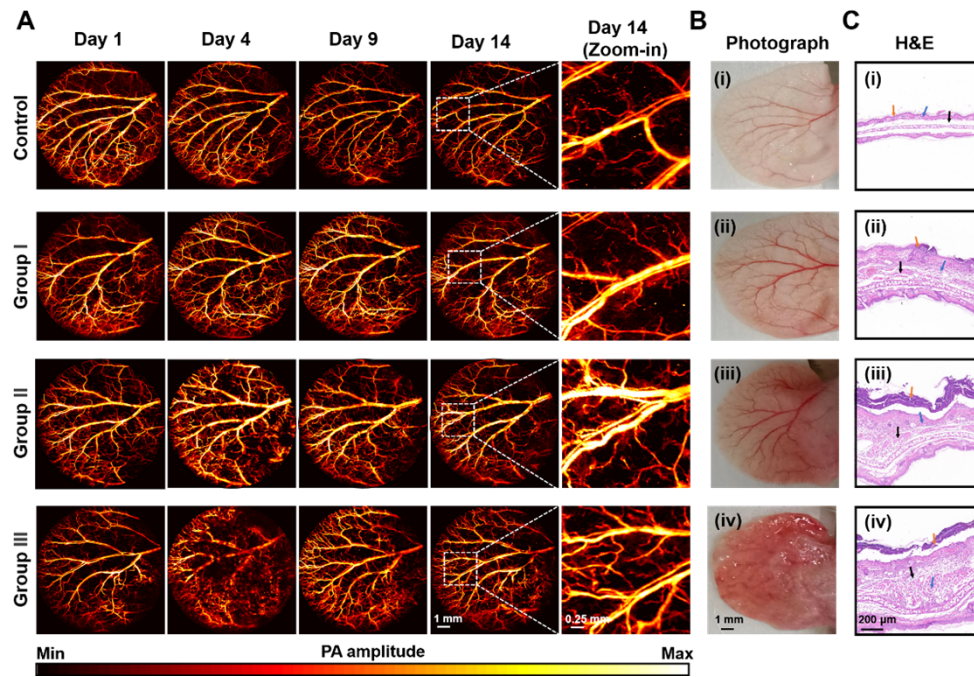
Fig. 3. *In vivo* longitudinal monitoring and verification with horizontal comparisons of TAP-induced ear inflammation. (A) OR-PAM images of TPA-induced ear inflammation with different concentrations on day 1, 4, 9 and 14 from the four experimental groups. The zoom-in images demonstrate the increasing number of tortuous vessels with larger TPA concentration. Each horizontal set of four pictures depicts the gradual healing process of ear inflammation. (B) Color photographs and (C) H&E staining histology sections for each group on day 4.

32.4%, p < 0.0001) among the experimental groups. Afterwards, the mean diameter undergoes a steeper decrease than the maximum diameter, which can be attributed to the autoimmune response that requires a considerable number of capillaries for oxygen supply. The gradual decrease of maximum vessel diameter suggests vasoconstriction of the central artery. Figure 4(A) (iii) indicates the change in tortuosity over the 14-day experimental period, with tortuosity increasing in the first 5-6 days and then gradually returning to the original value for groups I-III. In principle, higher concentrations of TPA result in more tortuous vasculature. Elevated blood vessel tortuosity is indicative of endothelial cell activation, pathological microvascular remodeling, and ischemia-induced arterialization in the collateral vascular system [18]. Figures 4(A) (iv-vii) demonstrate the variations in BN, VL, FD, and VAF, with their curve trends appearing relatively similar: an initial decrease during the first two days, followed by a gradual increase until reaching the maximum value, and finally, a gradual decrease to converge towards the baseline. The spatial distribution of capillary networks determines spatial oxygenation and nutrient delivery heterogeneity [18]. The reduction of the four parameters aligns with the disappearance of vasculature in OR-PAM images taken at identical time points, while an increase in these parameters marks the activation of an autoimmune effect to produce capillaries for enhanced oxygen and nutrient delivery. Figure 4(A) (viii) reflects the development of edema through the measurement of ear thickness. The thickness of edema increases in a dose-dependent manner with higher doses of TPA, as evidenced by the comparison between groups. The progression of edema involves an initial phase of increasing severity followed by a subsequent deceleration. Notably, while groups I-III display significant

changes in vessel parameters, the parameter values of the control group remained relatively stable throughout the observation period. In addition, horizontal comparisons between the final values of parameters depicted in Fig. 4(B) provide a more intuitive illustration of the inflammatory effect of TPA. The vessel parameters and the ear thickness displayed in Figs. 4(B) (i-viii) demonstrate significant differences ($p < 0.001$; $p < 0.0001$) between the model and the control groups. The above longitudinal and dynamic observation provides a comprehensive understanding of the development of TPA-induced inflammation and edema.
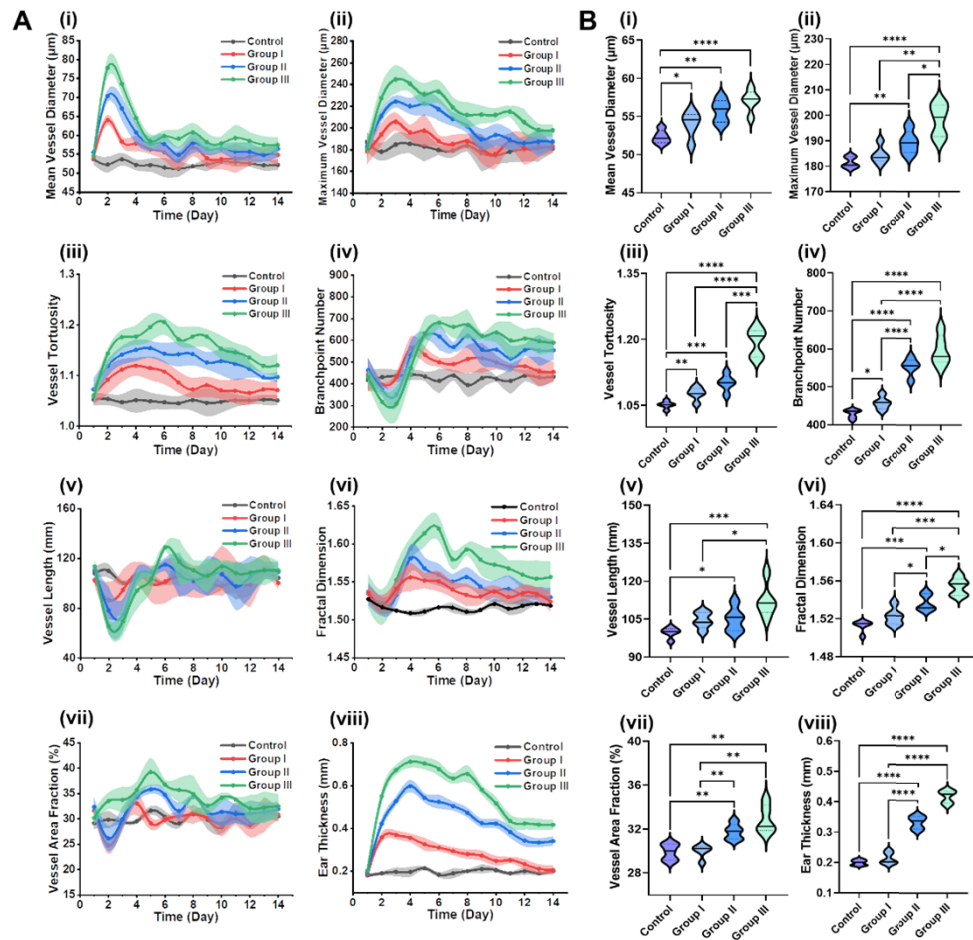
Fig. 4. Quantitative analysis of the changes of vascular parameters in TPA-induced ear inflammation. (A) The variation curves of eight quantitative parameters over the 14-day time in each experimental group, including (i) mean vessel diameter, (ii) maximum vessel diameter, (iii) vessel tortuosity, (iv) branchpoint number, (v) vessel length, (vi) fractal dimension, (vii) area fraction and (viii) ear thickness. (B) The quantitative comparisons of several vessel parameters and ear thickness on day 14 between different experimental groups. Dash area of variation curve in (A) represents standard deviations; The quantitative comparisons in (B) were represented by violin plots with quartile range (dotted) and median (bold); *, $p < 0.05$; **, $p < 0.01$; ***, $p < 0.001$; ****, $p < 0.0001$.
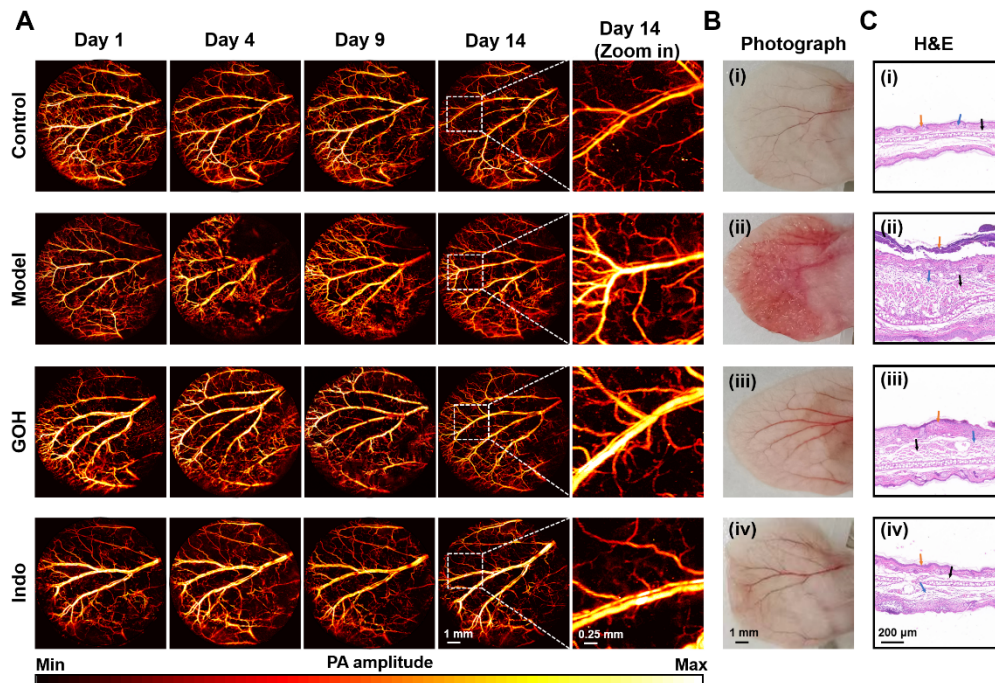
Fig. 5. *In vivo* longitudinal monitoring and verification with comparisons of the therapeutic effect of geraniol and indomethacin on TPA-induced ear inflammation. (A) Representative OR-PAM images on day 1, 4, 9 and 14 from the four different experimental groups. The zoom-in images on day 14 demonstrate the decrease of vessel density with the presence of treatment drugs. Each horizontal set of four images depicts the gradual healing process of ear inflammation. (B) Color photographs and (C) H&E staining histology sections of mice ears for each group on day 4.

3.2. Anti-inflammatory treatment for TPA-induced inflammation

We further utilized OR-PAM imaging to evaluate the impact of geraniol and indomethacin on TPA-induced inflammation. With the aid of the imaging module, we could rapidly acquire label-free OR-PAM images of mice ears. The structural information presented in the OR-PAM images can directly reflect the development of ear inflammation. Longitudinal OR-PAM imaging results of the different groups are depicted in Fig. 5(A). The results of the control group show that there is no significant change in the ear vascular network during the two-week monitoring. However, in the model group, the stimulation of TPA inflammatory drugs led to significant changes in the vascular network on day 4, and the inflammatory symptoms are still obvious until the end of the monitoring cycle. Compared to the model group, the OR-PAM results of GOH and Indo groups reveal minimal alterations in vascular structure during the initial stages of inflammation. Among them, the zoom-in images provide a more intuitive comparison of vessel density between the different groups, and the decrease in vessel density caused by therapeutic drugs can be observed. This is because after the application of anti-inflammatory drugs, the changes of microcirculatory and the increase of vascular permeability in postcapillary venules can be improved and inhibited respectively, which also indicates that the chemical mediators produced by TPA stimulation are effectively compressed. Figure 5(B) and Fig. 5(C) show the ear photographs and H&E staining sections of different groups on day 4, respectively. By integrating the results of the *in vivo* and *ex vivo* experiments on day 4 in Figs. 5(A)-(C), the anti-inflammatory

effects of geraniol and indomethacin can be cross-evaluated. As shown in Fig. 5(B), there is no severe redness, psoriasis, or hemorrhage in the mice ears of two treatment groups compared to the model group. At the same time, Fig. 5(C) (with the same arrow implications in Fig. 3(C)) shows that the extent of epidermal hyperplasia, tissue edema, and neutrophil infiltration is greatly attenuated and retarded compared to the model group. In addition, no distinct enriched accumulation of extracellular matrix was observed, suggesting alleviation of the fibrotic response to inflammatory conditions. These results indicate that the administration of geraniol and indomethacin can significantly reduce the number of inflammatory cells and the area of inflamed
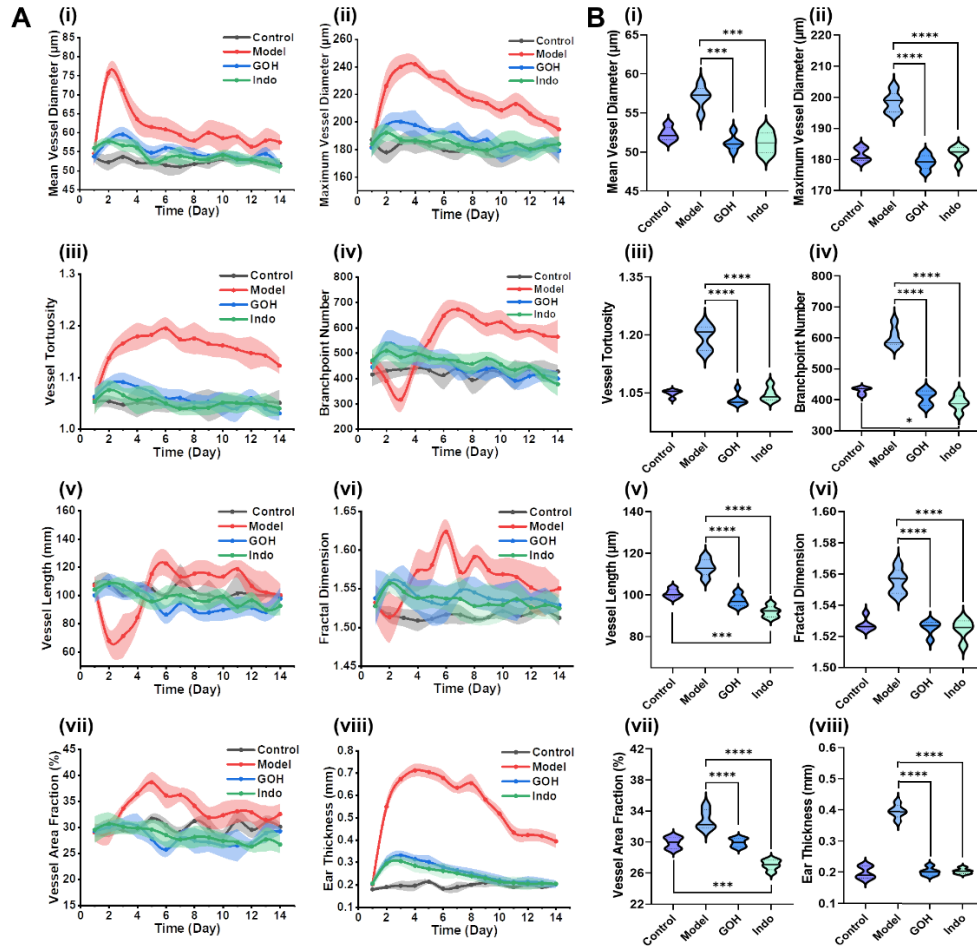
Fig. 6. Quantitative analysis of the vessel parameters variation of TPA-induced ear inflammation after applying therapeutic drugs. (A) The variation curves of eight quantitative parameters over the 14-day in different group, including (i) mean vessel diameter, (ii) maximum vessel diameter, (iii) vessel tortuosity, (iv) branchpoint number, (v) vessel length, (vi) fractal dimension, (vii) area fraction and (viii) ear thickness. There are control, model, GOH and Indo experimental groups, of which GOH and Indo group are treated with anti-inflammatory drugs geraniol and indomethacin, respectively. (B) The quantitative comparisons of several vessel parameters and ear thickness on day 14 between four experimental groups. Dash area of variation curve in (A) represents standard deviations. The quantitative comparisons in (B) are represented by violin plots with quartile range (dotted) and median (bold); *, $p < 0.05$; **, $p < 0.01$; ***, $p < 0.001$; ****, $p < 0.0001$.

tissue in the ears. Although residual pathological tissue is still observable compared to the control group, these findings still manifest the anti-inflammatory abilities of the drugs.

Subsequently, we obtained vessel parameters through OR-PAM image processing to evaluate the morphological and dynamic characterization of mice ear vasculatures. Quantitative analyses of vessel parameters reveal an immense increase in diameter and tortuosity in the model group on day 2, while the GOH and Indo groups exhibit a minor elevation that rapidly reverts to baseline levels, as illustrated in Figs. 6(A) (i-iii). For instance, the maximum increase in vessel tortuosity for the GOH and Indo groups is 3.2% and 2.1%, respectively, markedly lower than the model group (13.3%). Figures 6(A) (iv-vii) illustrate the progression of BN, VL, FD, and VAF, respectively. In addition to the differentiation in parameter magnitudes during day 6-14, the variations in the curve slopes between day 1-5 warrant attention. The model group exhibits a negative slope during the initial 2-3 days, transitioning to a positive slope thereafter, while the GOH and Indo groups display the inverse trend. The observed vacancy of the phase labeled by the disappearance of capillaries is attributed to the anti-inflammatory effect that inhibits blood clot formation, while the elevation in values is ascribed to the activation of autoimmune system generating capillaries. The reduction in edema size was confirmed by the decrease in ear thickness (Fig. 6(A) (viii)). Furthermore, vessel parameters following 14-day treatment are significantly lower than those observed in the model group, indicating a disparity in the therapeutic effects of the autoimmune system and anti-inflammatory drugs (Fig. 6(B)).

4.　Discussion

Cutaneous inflammation plays a pivotal role in both physiological and pathological conditions. Evaluating inflammatory processes can yield crucial insights into the associations between inflammatory processes and chronic or acute inflammatory dermatoses. In this study, we proposed a long-term noninvasive OR-PAM imaging and quantitative analysis approach to monitor and evaluate the TPA-induced inflammatory response and the therapeutic effect of anti-inflammatory drugs. The observations and analyses conducted not only corroborate the assessment at the physiological and cellular level reported in previous literatures, but also offer novel insights into inflammation monitoring. A preliminary hallmark of skin irritation and localized inflammation in the TPA model is characterized by an increase of VD1, VD2, VT, and ear thickness (Figs. 4(A) (i-iii), (viii)), concomitant with a decrease of BN, VL, FD, and VAF (Figs. 4(B) (iv-vii)). These findings suggest the acute production of proinflammatory cytokines and vascular aberrations. Within the first few days of the healing process, haemostasis will take place [29]. Blood clots will be formed to fill up the wound bed, serving as a provisional healing matrix and functioning as scaffolds for the migration of thrombocytes and leukocytes. This will cause the majority of small vessels to be completely occluded. The disappearance of small blood vessels results in the decrease of BN, VL, FD, and VAF as well as the disconnection and degradation of the vascular systems in groups III and IV on day 4 in Fig. 3. The subsequent phase of inflammation is marked by increasing VT, BN, VL, FD, VAF, and ear thickness (Figs. 4(A) (iii-viii)) with a decrease in diameter (Figs. 4(A) (i-ii)), satisfying the oxygen and nutritional demand for angiogenesis and autoimmune response. Ultimately, the decreasing trend of all parameters toward the baseline denotes the effect of the autoimmune system against inflammation. For the treatment experiment, geraniol and indomethacin greatly affect the aforementioned process by suppressing the increasing rate and amplitude of parameters, which is connected to restraining the over-production of inflammatory mediators. However, an outlier exists in the vessel area fraction of group III (Fig. 4(A) (vii)) in contrast to the remaining groups, which exhibits an upward trend. A plausible explanation for the phenomenon is that subcutaneous hemorrhage and vascular leakage are severe in the early stage of high-dose TPA-induced inflammation, resulting in a larger detected PA signal area and a larger vessel area fraction. The effect of blood occlusion is more significant than vascular permeability, resulting in a decreased value.

In the comparative analysis of final parametric values between groups, the approximate increase ratios for parameters in Figs. 6(B) (i-viii) are -10.5%, -7.3%, -7.6%, -29.2%, -15.2, -1.9%, -18.7% and -32.4%, respectively, when compared to the model group. The value of parameters for GOH and Indo groups are situated within the same interval as the control group, while a notable difference is observed between the model group and Indo group. A statistically significant difference ($p < 0.05$) is also observed between the control group and treatment groups in Figs. 6(B) (iv), (v), and (vii). The decrease in VL and VAF induced by indomethacin can be further elucidated by the artery-clogging process stimulated by nonsteroidal medicine. Geraniol, a prominent isoprenoid and a primary constituent of rose and palmarosa oil, as well as an active component in essential oils of lemon and ginger, exhibits minimal side effects on vessel parameters (Figs. 6(B) (iv), (v), and (vii)) and superior therapeutic efficacy compared to indomethacin [6].

Currently, available anti-inflammatory drugs primarily consist of steroidal anti-inflammatory drugs (SAIDs) and nonsteroidal anti-inflammatory drugs (NSAIDs). Long-term application of SAIDs induces hyperfunction of the adrenal cortex, resulting in symptoms such as amyotrophy, central obesity, and hypertension. Indomethacin-like NSAIDs also possess gastrointestinal and cardiovascular side effects [19]. Consequently, the development of safe and effective natural products as novel anti-inflammatory agents has emerged as a burgeoning research area in drug discovery. OR-PAM imaging with quantitative vessel analysis can reduce the requisite number of experimental animals in studies aimed at identifying natural anti-inflammatory medications.

The results demonstrate the potential of OR-PAM with quantitative analysis methods to supplant laborious histological procedures and offer the broad potential for noninvasive dermatological pathology diagnosis. Although the conducted methods and experiments validate the use of OR-PAM and the quantification methods in evaluating vascular structure and morphology, certain limitations persist. Two of the most critical functional vascular parameters, oxygen saturation of hemoglobin (sO_2) and blood flow, are significantly associated with tissue metabolism and vascular hemodynamics [30]. A dual-wavelength system with a high scanning speed can address these problems and achieve the simultaneous acquisition of structural and functional information. To realize clinical diagnosis, a substantial quantity of OR-PAM images at different inflammatory stages from various skin regions of the human body must be obtained. Different types of U-Net need to be trained to segment vasculature from diverse skin regions to ensure accuracy. Moreover, a novel system combined with selected vessel metrics and parameters should be developed to automatically decide the parameters to be quantified, while the weight of each parameter is set for precise analysis depending on different inflammatory types. These investigations would expedite the progress of OR-PAM for clinical inflammation applications.

5. Conclusion

In summary, we demonstrate the capability of noninvasive quantitative methods based on OR-PAM imaging to monitor TPA-induced cutaneous inflammation and evaluate the anti-inflammatory efficacy of geraniol and indomethacin. Two adjuvant modules were designed to ensure uniform inflammation and large-scale imaging. The algorithm developed based on U-Net enabled multi-parametric and precise assessment of vasculature, extracting parameters including VD1, VD2, VT, VAF, BN, and FD. Combining *in vivo* OR-PAM imaging with images of color photographs and histological sections to analyze the physiological conditions behind the vascular structural and parametric alterations can better bridge the morphological information with clinical diagnosis. In particular, our method shows great potential in noninvasive clinical quantification of the degree of inflammation and the effect of different therapeutic strategies.

References

1. M. Pasparakis, I. Haase, and F. O. Nestle, "Mechanisms regulating skin immunity and inflammation," Nat. Rev. Immunol. **14**(5), 289–301 (2014).
2. Z. Li, T. Li, C. Zhang, J.-S. Ni, Y. Ji, A. Sun, D. Peng, W. Wu, L. Xi, and K. Li, "A multispectral photoacoustic tracking strategy for wide-field and real-time monitoring of macrophages in inflammation," Anal. Chem. **93**(24), 8467–8475 (2021).
3. R. A. Swerlick and T. J. Lawley, "Role of microvascular endothelial cells in inflammation," J. Invest. Dermatol. **100**(1), S111–S115 (1993).
4. P.-S. Lee, Y.-S. Chiou, P.-Y. Chou, K. Nagabhushanam, C.-T. Ho, and M.-H. Pan, "3′-Hydroxypterostilbene Inhibits 7,12-Dimethylbenz[a]anthracene (DMBA)/12-O-tetradecanoylphorbol-13-acetate (TPA)-induced mouse skin carcinogenesis," Phytomedicine **81**, 153432 (2021).
5. M. Neagu, C. Constantin, C. Caruntu, C. Dumitru, M. Surcel, and S. Zurac, "Inflammation: A key process in skin tumorigenesis (review)," Oncol. Lett. **17**, 4068–4084 (2018).
6. Q. Khan, R. Khan, W. Qamar, A. Lateef, M. U. Rehman, M. Tahir, F. Ali, O. O. Hamiza, S. K. Hasan, and S. Sultana, "Geraniol attenuates 12-O-tetradecanoylphorbol-13-acetate (TPA)-induced oxidative stress and inflammation in mouse skin: Possible role of p38 MAP Kinase and NF-κB," Exp. Mol. Pathol. **94**(3), 419–429 (2013).
7. J. Rebling, M. Ben-Yehuda Greenwald, M. Wietecha, S. Werner, and D. Razansky, "Long-term imaging of wound angiogenesis with large scale optoacoustic microscopy," Adv. Sci. **8**(13), 2004226 (2021).
8. E. A. Csuka, S. C. Ward, C. Ekelem, D. A. Csuka, M. Ardigò, and N. A. Mesinkovska, "Reflectance confocal microscopy, optical coherence tomography, and multiphoton microscopy in inflammatory skin disease diagnosis," Lasers Surg. Med. **53**(6), 776–797 (2021).
9. M. A. Ilie, C. Caruntu, D. Lixandru, M. Tampa, S.-R. Georgescu, M.-M. Constantin, C. Constantin, M. Neagu, S. A. Zurac, and D. Boda, "In vivo confocal laser scanning microscopy imaging of skin inflammation: clinical applications and research directions (Review)," Exp. Ther. Med. **17**, 1004–1011 (2018).
10. G. Mahé, A. Humeau-Heurtier, S. Durand, G. Leftheriotis, and P. Abraham, "Assessment of skin microvascular function and dysfunction with laser speckle contrast imaging," Circ. Cardiovasc. Imaging **5**(1), 155–163 (2012).
11. C. M. Treu, O. Lupi, D. A. Bottino, and E. Bouskela, "Sidestream dark field imaging: the evolution of real-time visualization of cutaneous microcirculation and its potential application in dermatology," Arch. Dermatol. Res. **303**(2), 69–78 (2011).
12. M. Xu and L. V. Wang, "Photoacoustic imaging in biomedicine," Rev. Sci. Instrum. **77**(4), 041101 (2006).
13. J. Yao and L. V. Wang, "Photoacoustic microscopy," Laser Photonics Rev. **7**(5), 758–778 (2013).
14. Q. Chen, W. Qin, W. Qi, and L. Xi, "Progress of clinical translation of handheld and semi-handheld photoacoustic imaging," Photoacoustics **22**, 100264 (2021).
15. H. F. Zhang, K. Maslov, G. Stoica, and L. V. Wang, "Functional photoacoustic microscopy for high-resolution and noninvasive in vivo imaging," Nat. Biotechnol. **24**(7), 848–851 (2006).
16. Z. Li, P. He, Y. Xu, Y. Deng, Y. Gao, and S.-L. Chen, "In vivo evaluation of a lipopolysaccharide-induced ear vascular leakage model in mice using photoacoustic microscopy," Biomed. Opt. Express **13**(9), 4802–4816 (2022).
17. Y.-H. Liu, L. M. Brunner, J. Rebling, M. Ben-Yehuda Greenwald, S. Werner, M. Detmar, and D. Razansky, "Non-invasive longitudinal imaging of VEGF-induced microvascular alterations in skin wounds," Theranostics **12**(2), 558–573 (2022).
18. T. S. Rao, J. L. Currie, A. F. Shaffer, and P. C. Isakson, "Comparative evaluation of arachidonic acid (AA)- and tetradecanoylphorbol acetate (TPA)-induced dermal inflammation," Inflammation **17**(6), 723–741 (1993).
19. J.-Y. Wu, Y.-J. Chen, L. Bai, Y.-X. Liu, X.-Q. Fu, P.-L. Zhu, J.-K. Li, J.-Y. Chou, C.-L. Yin, Y.-P. Wang, J.-X. Bai, Y. Wu, Z.-Z. Wu, and Z.-L. Yu, "Chrysoeriol ameliorates TPA-induced acute skin inflammation in mice and inhibits NF-κB and STAT3 pathways," Phytomedicine **68**, 153173 (2020).
20. Z. Yang, J. Chen, J. Yao, R. Lin, J. Meng, C. Liu, J. Yang, X. Li, L. Wang, and L. Song, "Multi-parametric quantitative microvascular imaging with optical-resolution photoacoustic microscopy in vivo," Opt. Express **22**(2), 1500–1511 (2014).
21. B. A. Corliss, C. Mathews, R. Doty, G. Rohde, and S. M. Peirce, "Methods to label, image, and analyze the complex structural architectures of microvascular networks," Microcirculation **26**(5), e12520 (2019).

22. W. Qi, T. Li, C. Zhang, F. Liu, J. Wang, D. Chen, X. Fang, C. Wu, K. Li, and L. Xi, "Light-controlled precise delivery of NIR-responsive semiconducting polymer nanoparticles with promoted vascular permeability," Adv. Healthcare Mater. **10**(19), 2100569 (2021).

23. O. Ronneberger, P. Fischer, and T. Brox, "U-Net: convolutional networks for biomedical image segmentation," in *Medical Image Computing and Computer-Assisted Intervention – MICCAI 2015*, N. Navab, J. Hornegger, W. M. Wells, and A. F. Frangi, eds., Lecture Notes in Computer Science (Springer International Publishing, 2015), pp. 234–241.

24. D. P. Kingma and J. Ba, "Adam: A Method for Stochastic Optimization," arXiv, arXiv:1412.6980 (2017).

25. K. Ren, L. Chang, M. Wan, G. Gu, and Q. Chen, "An improved U-net based retinal vessel image segmentation method," Heliyon **8**(10), e11187 (2022).

26. T. T. Mai, S. W. Yoo, S. Park, J. Y. Kim, K.-H. Choi, C. Kim, S. Y. Kwon, J.-J. Min, and C. Lee, "In vivo quantitative vasculature segmentation and assessment for photodynamic therapy process monitoring using photoacoustic microscopy," Sensors **21**(5), 1776 (2021).

27. G. Reishofer, K. Koschutnig, C. Enzinger, F. Ebner, and H. Ahammer, "Fractal dimension and vessel complexity in patients with cerebral arteriovenous malformations," PLoS One **7**(7), e41148 (2012).

28. M. Helmberger, M. Pienn, M. Urschler, P. Kullnig, R. Stollberger, G. Kovacs, A. Olschewski, H. Olschewski, and Z. Bálint, "Quantification of tortuosity and fractal dimension of the lung vessels in pulmonary hypertension patients," PLoS One **9**(1), e87515 (2014).

29. N. X. Landén, D. Li, and M. Ståhle, "Transition from inflammation to proliferation: a critical step during wound healing," Cell. Mol. Life Sci. **73**(20), 3861–3885 (2016).

30. N. Sun, A. C. Bruce, B. Ning, R. Cao, Y. Wang, F. Zhong, S. M. Peirce, and S. Hu, "Photoacoustic microscopy of vascular adaptation and tissue oxygen metabolism during cutaneous wound healing," Biomed. Opt. Express **13**(5), 2695–2706 (2022).